Macromolecules

pubs.acs.org/Macromolecules Article

Hydrogen-Bonded Ultrathin Porous Polyamide Membrane for High Flux H_2/CO_2 Separation

Yu Zhang, Feng Zhang, Shuqi Liu, Lele Guo, Zhenggong Wang,* and Jian Jin

Cite This: *Macromolecules* 2024, 57, 9419−9428 Read Online

ACCESS | Metrics & More | Article Recommendations | Supporting Information

ABSTRACT: High-performance polymer-based H_2/CO_2 separation membranes are attractive for sustainable blue hydrogen production. However, achieving high-flux separation remains a challenge, as H_2 and CO_2 have similar diffusion rates within the polymer. In this work, hydrogen-bonded polyamide (PA) network membranes are synthesized through interfacial polymerization involving Tröger's base diamine (TBDA) and 1,3,5-benzenetricarbonyl trichloride, aiming to enhance the efficiency of H_2/CO_2 separation. Incorporating the contorted TBDA unit into the PA structure enhances microporosity, which, in turn, boosts the H_2 permeance of the PA membrane. Notably, the presence of numerous intermolecular hydrogen bonds between N atoms in the TBDA and H atoms in the amide groups helps to restrict the pore size further, thereby improving the H_2/CO_2 selectivity of the membrane. The resulting PA membrane demonstrates an outstanding H_2/CO_2 selectivity of 23.5, coupled with a high H_2 permeance of 160 gas permeation unit (GPU), significantly exceeding the current upper bound. Additionally, our PA membranes maintain a stable H_2/CO_2 selectivity of approximately 21.5 and a H_2 permeance of around 160 GPU over 100 h, indicating excellent long-term stability. These findings suggest that the development of such advanced polymer membranes could pave the way for more efficient and sustainable blue hydrogen production, overcoming existing limitations in gas separation technologies.

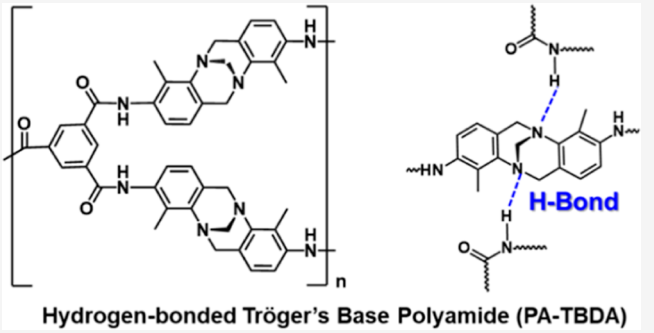

INTRODUCTION

Hydrogen is a crucial energy carrier with a significant potential for reducing carbon emissions. It produces approximately three times the combustion heat of gasoline for the same mass, all while generating zero emissions.[1−3] Producing a significant amount of hydrogen energy directly from natural sources presents considerable challenges. Presently, around 90% of hydrogen is generated through methods like natural gas reforming and coal gasification.[4−7] These processes inevitably produce carbon dioxide as a byproduct, making CO_2 capture during H_2 purification a critical step for ensuring the economic viability of these methods. Currently, H_2 can be purified using one or a combination of three primary methods: pressure swing adsorption, fractional and cryogenic distillation, and membrane separation.[8−10] Membrane separation is seen as a promising method for H_2 purification due to its high energy efficiency, lower investment costs, and simplicity of operation.[11−13] Polymer membranes, in particular, have garnered significant interest as they offer favorable mechanical properties, low costs, ease of processing, and scalability.[14−16] Gas permeability (P) is the product of gas solubility (S) and diffusivity (D; $P = S \times D$). In polymer membranes, polar CO_2 molecules typically exhibit higher solubility than H_2 molecules, while H_2 with its smaller molecule size, has a higher diffusion coefficient compared to CO_2.[17] As a result, the permeabilities of H_2 and CO_2 in polymer membranes are often quite similar, making it very challenging to design polymer membranes that achieve high H_2/CO_2 separation performance.[18]

Currently, H_2/CO_2 selective polymer membranes are often made from dense glassy polymers like polybenzimidazole (PBI) to achieve higher selectivity.[19−21] PBI has a very low free volume due to its tight chain packing, which leads to low H_2 permeability[22−25] typically in the range of several barrer (1 barrer = 1×10^{-10} cm^3 (STP) cm cm^{-2} s^{-1} $cmHg^{-1}$). Additionally, PBI is challenging to fabricate into thin film membranes because of its low solubility and processability. Recently, thin-film membranes made using interfacial polymerization (IP) have received significant attention for high flux H_2/CO_2 separation.[26] Pinnau et al. demonstrated defect-free, cross-linked polyamide (PA) thin film composite membranes with thickness ranging from 170 to 480 nm. These membranes were prepared using *p*-phenylenediamine, *m*-phenylenediamine, and piperazine in reaction with trimesoyl, achieved through extended reaction times (∼5 min) and elevated

Received: April 28, 2024
Revised: September 9, 2024
Accepted: September 10, 2024
Published: September 23, 2024

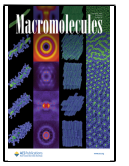

https://doi.org/10.1021/acs.macromol.4c00967
Macromolecules 2024, 57, 9419−9428

temperature (100 °C). The thin film composite membranes exhibited H_2 permeance values ranging from 25 to 37 gas permeation unit (GPU) (1 GPU = 1×10^{-6} cm^3 (STP) cm^{-2} s^{-1} $cmHg^{-1}$) and achieve high H_2/CO_2 selectivity between 10 and 14.[27] This method effectively eliminates defects and enhances the H_2/CO_2 selectivity. However, the planar structures of phenylenediamines result in tightly packed molecular chains and low microporosity, which limits the gas permeance of the resulting membrane. Livingston et al. introduced contorted phenols, such as spiro-structured 5,5′,6,6′-tetrahydroxy-3,3,3′,3′-tetramethylspirobisindane and cardo-structured 9,9-bis(4-hydroxyphenyl) fluorene, to create polyarylate membranes with improved microporosity through IP. These membranes demonstrated enhanced H_2 permeance ranging from 71 to 78 GPU, and H_2/CO_2 selectivity between 8 and 12[28] (Table 1). Incorporating contorted structures can increase the microporosity and gas permeance of the membrane, but the looser packing of polymer chains may also reduce the membrane's selectivity. Overall, thin IP-based polymer membranes offer higher H_2 permeance compared to traditional polymer materials, demonstrating the significant potential for H_2/CO_2 separation. However, there is a gap in IP-polymer membrane materials that effectively balances H_2 permeance, H_2/CO_2 selectivity, and the required durability for the separation process.

Table 1. Comparison of Mixed-Gas Permeance and Selectivity of IP-Based Polymer Membranes with an Optimally Structured PA-TBDA Membrane

membrane	permeance (GPU) H_2	permeance (GPU) CO_2	selectivity H_2/CO_2
PIP-TMC-KRO[27]	37.4	3.6	10.2
PPD-TMC-KRO[27]	32.6	2.9	11.2
MPD-TMC-KRO[27]	25.8	1.8	14.3
PAR-BHPF/PTMSP[28]	78.4	9.2	8.5
PAR-TTSBI/PTMSP[28]	71.2	5.7	12.5
PA-TBDA (this work)	160	6.8	23.5

Rationally controlling the internal pore structure of the polymer through molecular structure design is considered crucial for enhancing separation performance.[29−32] In this work, hydrogen-bonded PA network membranes are created through IP of Tröger's base diamine (TBDA) and 1,3,5-benzenetricarbonyl trichloride (TMC). Tröger's base (TB), a bridged bicyclic diamine known as 2,8-dimethyl-6*H*,12*H*-5,11-methanodibenzo[*b*,*f*][1,5]diazocine, was first identified by Julius Tröger in 1887.[33] TB has been utilized in a range of applications, including receptors, molecular torsion balances, ligands in asymmetric catalysis, and drug candidates.[34] Due to its rigid V-shaped amine structure, TB was subsequently found to be effective in constructing polymer for gas separation, as demonstrated by Mckeown, Guiver, and our research groups.[35−37] The contorted TB structure enhances the microporosity and increases the gas permeance of the resulting PA membrane. Additionally, interchain hydrogen bonds form between the nitrogen atoms of the tertiary amine in TB and the hydrogen atoms in the amide groups. The additional hydrogen bonds enhance interchain interaction and restrict pore size, thereby improving the membrane's molecular sieving properties. The synergistic design of the membrane's micropore structure results in simultaneous improvements in H_2 permeance and H_2/CO_2 selectivity compared to traditional IP-based PA membranes. The overall separation performance of the resulting porous PA membranes significantly surpasses the current upper bound for polymers, demonstrating their immense potential for hydrogen purification.

MATERIALS AND METHODS

Materials. Polyimide (P84, M_w = 127 K, M_n = 65 K) was purchased from HP-T Höglmeier Polymer-Tech Verwaltungs-GmbH. Poly [1-(trimethylsilyl)-1-propyne] (PTMSP) was purchased from Bide Pharmatech Co., Ltd. 1,3,5-benzenetricarbonyl trichloride (TMC, 99.0%) was purchased from J&K Scientific Ltd. 2-methyl-3-nitroaniline (>98.0%) was purchased from Tokyo Chemical Industry Co., Ltd. Hydrazine hydrate (>98.0%) was purchased from Beijing InnoChem Science & Technology Co., Ltd. Piperazine (PIP, >99.0%) was purchased from Hebei Bailingwei Super Fine Material Co., Ltd. Triethylamine (>99.5%), trifluoroacetic acid (AR), and *m*-phenylenediamine (MPD, 99.5%) were provided by Aladdin Industrial Corporation. Ethanol absolute (99.7%) and sodium hydroxide (AR) were purchased from Sinopharm Chemical Reagent Co., Ltd. Polyethylene glycol 400, *N*,*N*-dimethylformamide (DMF, ≥99.5%), *n*-hexane (≥97.0%), and trichloromethane (≥99.0%) were purchased from Chinasun Specialty Products Co., Ltd. Isopropyl alcohol (IPA, 99.5%) was purchased from Shanghai Merrill Trading Co., Ltd. Paraformaldehyde (AR), palladium/carbon (10.0% Pd), and 1,6-hexamethylenediamine (99.0%) were purchased from Shanghai Macklin Biochemical Co., Ltd.

Preparation of TBDA Monomer. The 3,9-diamino-4,10-dimethyl-6*H*,12*H*-5,11-methanodibenzo[1,5]diazocine (TBDA) was synthesized as our previous reported work.[38,39] First, under the condition of the ice bath, 12 g of 2-methyl-3-nitroaniline was dissolved into 150 mL of trifluoroacetic acid, and then 4.98 g of paraformaldehyde was added to dissolve and obtain a dark brown mixture. The reaction was stirred at room temperature for 2 days under nitrogen conditions. The resulting reaction product was poured into 200 mL of pure water and stir thoroughly. Then, 340 mL 6 mol·L^{-1} sodium hydroxide solution was slowly added to adjust pH to 8.5−9. The obtained yellow powder was then refluxed in 300 mL of acetone for 1 h. The resulting mixture was placed in a refrigerator at −20 °C and let it settle overnight. The product was filtered with a yield of 83%.

Under nitrogen conditions, 5 g of yellow solid obtained in the first step was dispersed into 100 mL of ethanol, and 0.5 g of palladium/carbon was added to the dispersion solution, and the mixture was heated to reflux. Then, 10 mL of hydrazine hydrate was added to the mixture. The mixture was refluxed overnight, the reaction liquid was filtered when it was hot, and the resulting filtrate was concentrated to half under reduced pressure. The obtained solution was added into 100 mL of water, and then the white powder was filtered and vacuum-dried at 60 °C, yield: 92%. ^{1}H NMR (400 MHz, DMSO-d_6): δ ppm: 6.46 (d, J = 8.0 Hz, 2H), 6.33 (d, J = 8.0 Hz, 2H), 4.60 (s, 4H), 4.37 (d, J = 16.0 Hz, 2H), 4.13 (s, 2H), 3.68 (d, J = 16.0 Hz, 2H), 2.06 (s, 6H). The ^{1}H NMR spectrum of the TBDA monomer is shown in Figure S1.

Preparation of PA Membranes. The XP84 support membranes were prepared by the nonsolvent-induced phase inversion method according to our previous report.[40,41] The XP84 membranes were cut into suitable sizes of approximately 4 × 4 cm^2 and attached to the silicon wafer. Initially, a chloroform solution containing 0.5% PTMSP was spin-coated as the gutter layer. Subsequently, the membrane was spin-coated with a solution of TMC in *n*-hexane, followed by a solution of TBDA in ethanol/water (1:5, v/v) with the addition of 200 mg/10 mL of triethylamine to promote dissolution. The solution was subjected to ultrasonic treatment until it was homogeneous. The spin coating parameters used were 2000 r·min^{-1} for 60 s. After allowing the membranes to rest overnight, they were placed in an oven at 60 °C for 2 h to allow for solvent evaporation.

Preparation of Freestanding Nanofilm Powders. The support-free water/*n*-hexane interface was utilized to prepare the

https://doi.org/10.1021/acs.macromol.4c00967
Macromolecules 2024, 57, 9419−9428

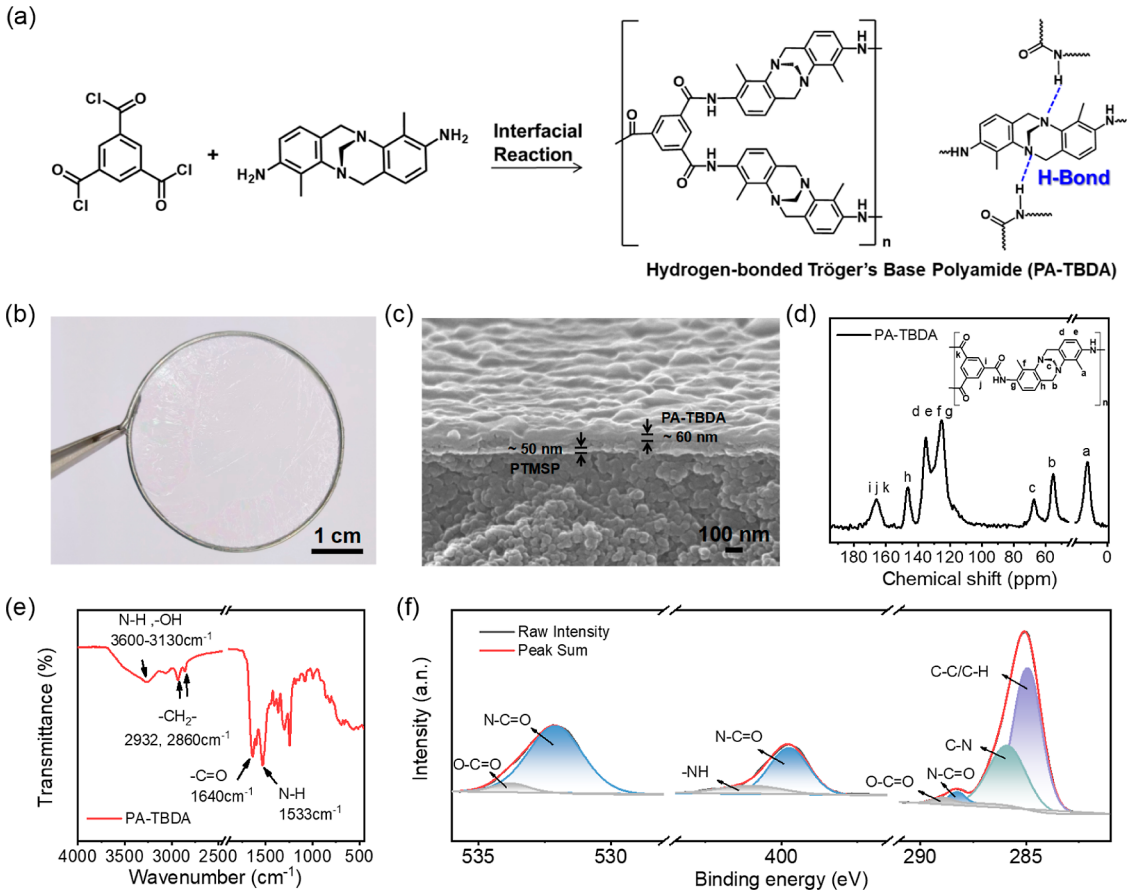

Figure 1. Synthesis and structural characterization of PA nanofilms. (a) Schematic of IP between TBDA and TMC monomers. (b) Photograph of PA-TBDA nanofilm on steel wire lasso. (c) FE-SEM surface image of PA-TBDA membrane. (d) ^{13}C NMR spectrum, (e) ATR-IR spectrum, and (f) high-resolution XPS spectra of C 1s, N 1s, and O 1s regions for PA-TBDA membranes.

freestanding nanofilms through IP. A 200 mL of 1 mg·mL^{-1} TBDA and TMC solutions was sequentially added into a container and stirred with magnets for 10 min. The resulting PA solid was collected and placed in 100 mL of *n*-hexane for 2 h of ultrasonic treatment to remove the unreacted TMC monomer. Next, the solids were collected and transferred them to 100 mL of water for ultrasonic treatment to remove the unreacted TBDA monomer. Finally, the PA solids were collected and subjected them to a vacuum oven at 60 °C for 24 h, followed by 100 °C for 10 h. The field emission scanning electron microscopy (FE-SEM) image of the freestanding PA-TBDA nanofilm powders is shown in Figure S2.

Characterization. The surface and cross-sectional morphologies were characterized by FE-SEM (Regulus 8230, Hitachi, Japan), and the acceleration voltage was 15 kV. After being dried, the film was plated with gold at 10 mA and 70 s by a plasma sputter to increase the conductivity. ^{13}C solid-state nuclear magnetic resonance spectra (^{13}C NMR) of PA powders were measured on a BRUKER AVANCE NEO 400WB. The thermal stability of PA was performed in the N_2 atmosphere using thermal gravimetric analysis (TG/DTA 6200), the temperature range between 40 and 800 °C with a heating rate of 10 °C/min. Fourier transform infrared (FTIR) spectroscopy was recorded at 400−4000 cm^{-1} on a Nicolet 6700 spectrometer. The surface elements (C, N, and O) of the selective layer of PA were analyzed semiquantitatively by X-ray photoelectron spectroscopy (XPS, EXCALAB 250XI). Bruker D8 ADVANCE X-ray diffractometer was used to characterize the *d*-spacing of the polymer chain of the membrane. The H_2 and CO_2 (273 K) adsorption experiments were analyzed on a Quantachrome Autosorb, IQ-MP at 273 K. All samples were activated thoroughly at 120 °C under a high vacuum before measurements. The pore size distribution was calculated by the density functional theory (DFT) model. The apparent surface area was calculated by the multipoint (Brunauer−Emmett−Teller (BET)) method from CO_2 adsorption data.

Membrane Performance Test. The gas separation performance of the membranes was evaluated by mixed gas. The 50:50 (vol/%) H_2 and CO_2 gas mixture with a total gas velocity of 60 mL·min^{-1} was used as feed. Argon (Ar) with a gas velocity of 10 mL·min^{-1} was used as sweep gas, and the permeate side's pressure was kept atmospheric. The steady-state feed, retentate, and permeate compositions were recorded by online gas chromatography equipped with a thermally conductive detector.

The gas permeance of component i (P_i) is calculated by eq 1

$$P_i = \frac{N_i}{\Delta p_i \cdot A} \tag{1}$$

Where N_i is the permeate rate of component i (mol s^{-1}), A is the membrane area, and Δp_i is the partial pressure difference of component i across the membrane. Here, the GPU is used as the unit of permeance, where 1 GPU = 1 × 10^{-6} cm^3 (STP) cm^{-2} s^{-1} cmHg^{-1}.

The gas separation factor (α_{H_2/CO_2}) is calculated by eq 2

$$\alpha_{H_2/CO_2} = \frac{y_{H_2}/y_{CO_2}}{x_{H_2}/x_{CO_2}} \tag{2}$$

where y_{H_2} (x_{H_2}) and y_{CO_2} (y_{CO_2}) are the molar fractions of H_2 and CO_2 in permeate (feed), respectively. The x is the mole fraction of the gas on the input side.

https://doi.org/10.1021/acs.macromol.4c00967
Macromolecules 2024, 57, 9419−9428

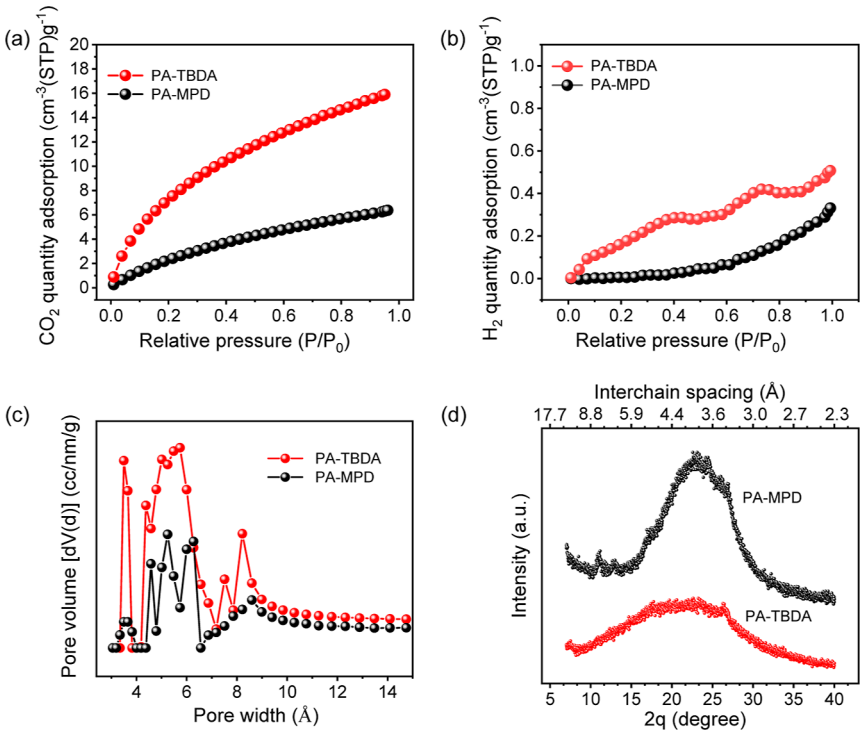

Figure 2. Characterization of microporous structure in PA membranes. (a) CO_2 and (b) H_2 adsorption isotherms of freestanding PA membranes at 273 K. (c) Pore size distribution of PA membranes derived from CO_2 adsorption, calculated using the DFT method. (d) WAXD pattern of freestanding PA membranes.

RESULTS AND DISCUSSION

The ultrathin PA selective layer was created on the XP84 support membrane through IP involving TBDA and TMC, as depicted in the schematic diagram in Figure 1a. To ensure the membrane was free of defects, a PTMSP layer was initially applied as a "gutter layer" by spin-coating it onto the XP84 support membrane.[42,43] To achieve a uniform monomer distribution, TMC and TBDA monomers were individually deposited onto the substrate using spin-coating. The resulting interfacial polymer is referred to as PA-TBDA. A significant feature of the PA-TBDA, PA is the formation of a strong hydrogen bond between the amide and TB groups. Figure 1b shows the durable and flexible PA-TBDA nanofilm supported by a 4 cm diameter steel ring. The PA nanofilm, supported by PTMSP, exhibits a colorless, transparent surface. The FE-SEM image of the PA membranes, shown in Figure 1c, reveals the characteristic ridge-and-valley structure and confirms the absence of defects. The thicknesses of selective layer and gutter layer are approximately 60 and 50 nm, respectively. These findings confirm the successful fabrication of the PA-TBDA layer on the surface of the XP84 support membrane. XP84 membrane, covered solely by a PTMSP gutter layer, exhibited a H_2 permeance of 2×10^4 GPU and a H_2/CO_2 selectivity of 1.4, demonstrating that the gutter layer does not impact the separation performance of the selective layer. The chemical structure of the PA membranes was analyzed by using ^{13}C NMR and attenuated total reflection-IR (ATR-IR) spectroscopy. The assignment of chemical shifts for carbon atoms to their respective chemical groups in the ^{13}C NMR spectrum is illustrated in Figure 1d. The peaks observed around 55 and 67 ppm correspond to carbon atoms within the TB group. As depicted in Figure 1e, the adsorption bands at 1640 and 1533 cm^{-1} are attributed to C═O stretching and N−H bending, respectively. The adsorption band within the range 3600−3130 cm^{-1} corresponds to the adsorption bands of the O−H and N−H stretching. As shown in Figure 1f, the peak at 399.7 eV in the XPS spectrum is attributed to the amide bond (N−C═O) in the PA. The characterizations presented above confirm the successful fabrication of the PA-TBDA membrane. Additionally, the thermal stability was assessed using thermogravimetric analysis (TGA). As illustrated in Figure S4, the decomposition temperature at 10% weight loss reaches up to 415 °C, indicating excellent thermal stability.

To gain deeper insights into the microstructure of PA-TBDA, physisorption and wide-angle X-ray diffraction (WAXD) characterizations were performed. For comparison, the same characterization techniques were applied to PA-MPD, which was synthesized using TMC and MPD. The H_2 and CO_2 adsorption properties of the polymers were evaluated through physisorption measurements conducted at 273 K.[44,45] As illustrated in Figure 2a, the CO_2 adsorption capacities of the PA-TBDA and PA-MPD membranes were found to be 15.9 and 6.4 $cm^3 \cdot g^{-1}$, respectively. The calculated BET surface area of PA-TBDA (147.8 $m^2 \cdot g^{-1}$) is significantly greater than that of PA-MPD (73.5 $m^2 \cdot g^{-1}$), indicating that incorporation of the contorted TBDA monomer effectively enhanced the surface area of the PA membranes. As depicted in Figure 2b, the H_2 adsorption amounts for both membranes are extremely low, suggesting that there is minimal interaction between the polymers and H_2 molecules. As illustrated in Figure 2c, the membranes exhibit hierarchical pore structures, including microporosity, ultramicroporosity, and submicroporosity, with pore sizes in the range of 7−9, 4−7, and <4 Å, respectively.[46] The peak intensity of the PA-TBDA membranes is significantly higher than that of the PA-MPD membranes

https://doi.org/10.1021/acs.macromol.4c00967
Macromolecules 2024, 57, 9419−9428

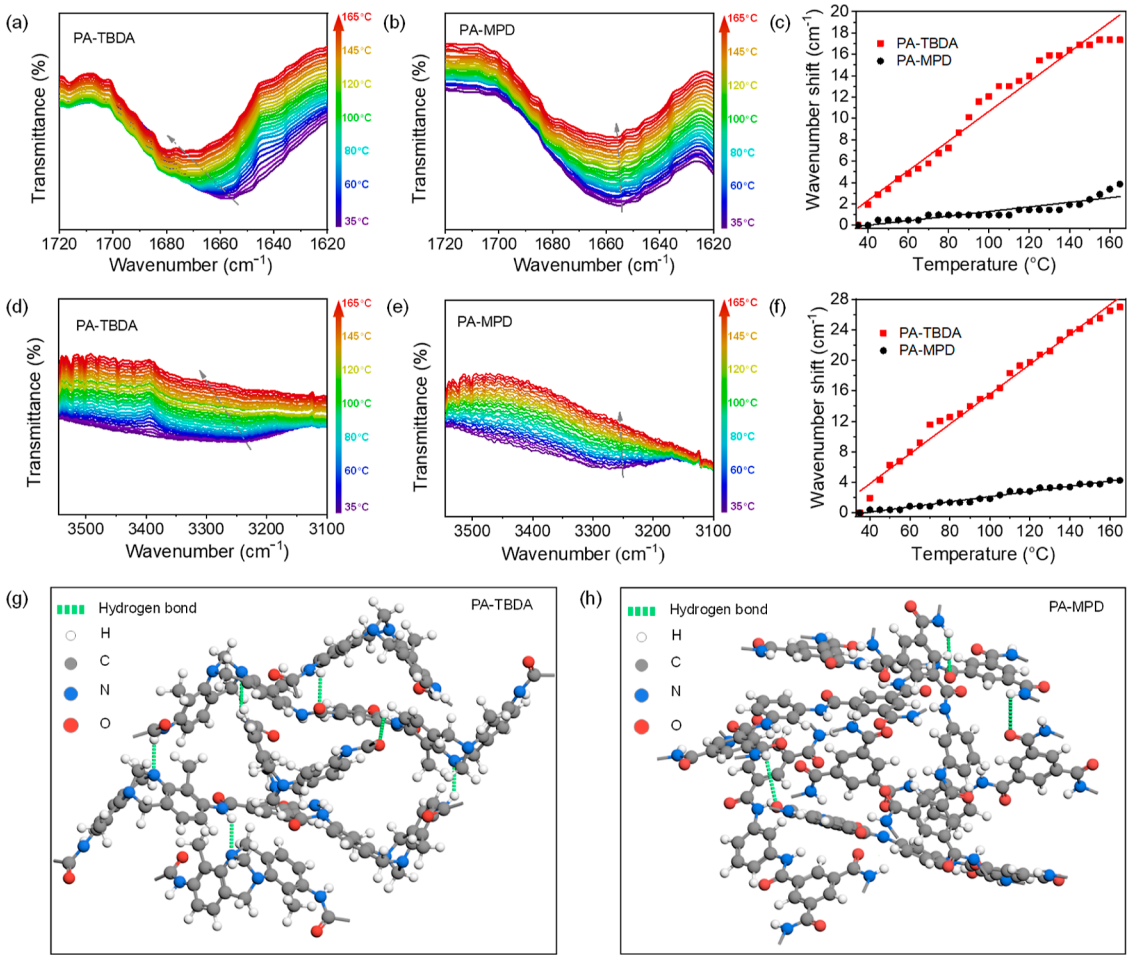

Figure 3. Hydrogen bonding in PA membranes. (a,b) Temperature-dependent infrared reflection spectra showing C═O stretching peaks for freestanding PA-TBDA and PA-MPD nanofilms. (c) Temperature-induced wavenumber shifts of C═O stretching vibration peaks for both nanofilms. (d,e) Temperature-dependent infrared reflection spectra of O−H and N−H stretching vibrations for freestanding PA-TBDA and PA-MPD nanofilms. (f) Wavenumber shifts of O−H and N−H stretching vibration peaks as a function of temperature for the two nanofilms. (g,h) Illustrations of hydrogen bonds in PA-TBDA and PA-MPD polymer models, optimized through energy minimization calculations.

across each pore range, indicating that the PA-TBDA membranes have enhanced microporosity. The X-ray diffraction profiles of the two polymer membranes exhibit a relatively broad peak at $2\theta \approx 10-30°$, as shown in Figure 2d, characteristic of their amorphous structures. The *d*-spacing, calculated using Bragg's equation,[47,48] was approximately 4.0 Å for PA-TBDA and 3.8 Å for PA-MPD. Compared to PA-MPD, PA-TBDA exhibits a broader half-peak width and lower peak intensities, suggesting that the incorporation of the rigid and contorted TBDA monomer disrupts the stacking of PA chains, leading to an increase in the amorphous phase and a larger average interlayer spacing.

Temperature-dependent IR reflection spectroscopy was conducted to verify the enhanced H-bonding in the PA-TBDA membrane. For comparison, the changes in wavenumber were also examined in the PA-MPD membrane. IR data were recorded at 5 °C intervals as the temperature increased. As shown in Figure 3a,d, with a temperature rising from 35 to 165 °C, the stretching vibration of the C═O group in the PA-TBDA membrane shifts from 1656 to 1673 cm^{-1}, while the stretching vibrations of the O−H and N−H groups shift from 3241 to 3268 cm^{-1}. As depicted in Figure 3b,e, for the PA-MPD membrane, the stretching vibration of the C═O group shifts from 1655 to 1659 cm^{-1}, and the stretching vibrations of the O−H and N−H groups shift from 3241 to 3246 cm^{-1} as the temperature increases from 35 to 165 °C. Additionally, the intensity of these peaks progressively decreases with increasing temperature. The red shift in the wavenumber and the weakness of the IR peaks with temperature variations suggest the presence of strong hydrogen bonding in PA-TBDA.[49,50] Figure 3c,f summarizes the wavenumber shifts of the C═O stretching adsorption peaks and the O−H and N−H stretching adsorption peaks for the two membranes with temperature changes. The adsorption peaks at 35 °C are used as the reference point. For PA-TBDA, the rate of increase for the C═O stretching vibration peak is 0.14 cm^{-1}/°C, and for the O−H and N−H stretching vibration peaks, it is 0.20 cm^{-1}/°C. In contrast, PA-MPD exhibits much lower rates of increase with 0.02 cm^{-1}/°C for the C═O stretching vibration and 0.03 cm^{-1}/°C for the O−H and N−H stretching vibrations. These results confirm that the PA-TBDA nanofilms exhibit sufficiently stronger H-bonding interactions. This suggests that the benzodiazocinic core of the TBDA monomer enhances hydrogen bonding within the PA network. Figure 3g,h illustrates the distribution of hydrogen bonds in PA-TBDA and PA-MPD, respectively. The PA-TBDA nanofilm exhibits a higher density of hydrogen bonds, highlighting the enhanced H-bonding interactions.

https://doi.org/10.1021/acs.macromol.4c00967
Macromolecules 2024, 57, 9419−9428

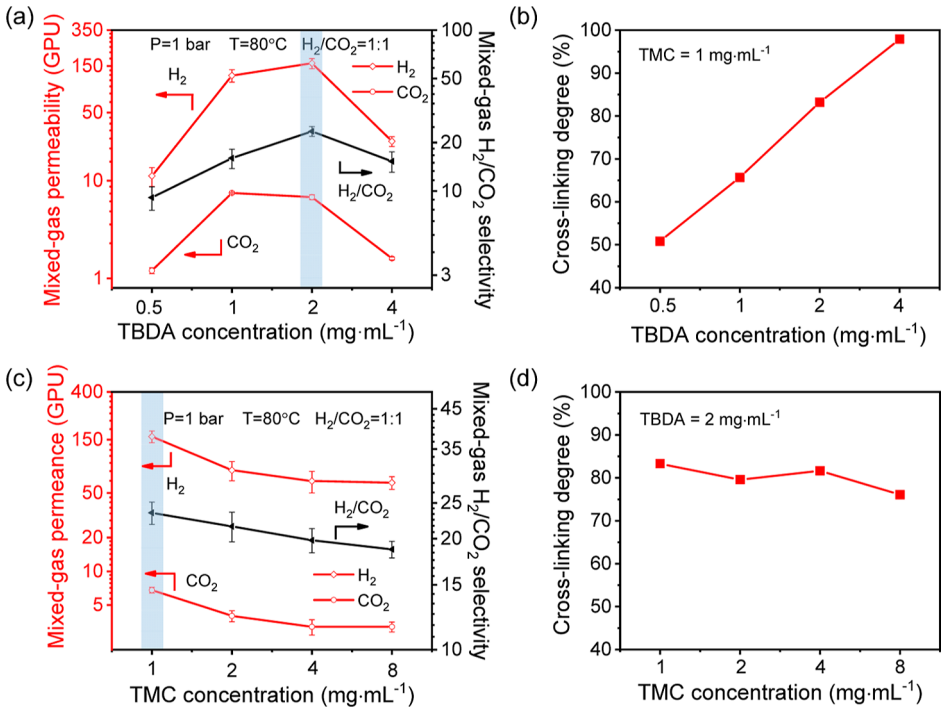

Figure 4. Optimization of membrane preparation conditions. The H_2/CO_2 separation performance of the PA-TBDA membranes was evaluated under various monomer concentrations to determine optimal conditions. With a fixed TMC concentration of 1.0 mg·mL^{-1} and increasing TBDA concentrations from 0.5 to 4.0 mg·mL^{-1}: (a) H_2/CO_2 mixed gas separation performance and (b) corresponding cross-linking degree in the PA-TBDA membranes fabricated by various TBDA concentrations. When the TBDA concentration was fixed at 2.0 mg·mL^{-1}, and the TMC concentration was varied from 1.0 to 8.0 mg·mL^{-1}: (c) H_2/CO_2 mixed gas separation performance and (d) corresponding cross-linking degree in the PA-TBDA membranes fabricated by various TMC concentrations.

The H_2/CO_2 separation performance of the PA-TBDA membranes was optimized by adjusting both the monomer concentration and the membrane thickness. The gas permeation properties of the prepared membranes were elevated at 80 °C, 1 bar using a 50:50 (vol/%) H_2/CO_2 mixed gas feed. As shown in Figure 4a, with the TMC concentration kept constant at 1.0 mg·mL^{-1}, increasing the TBDA concentration from 0.5 to 2.0 mg·mL^{-1}, resulted in an increase in the H_2/CO_2 selectivity of the membrane from 9.1 to 23. As shown in Figure S6, the thickness of the selective layer increased from 60 to 95 nm, as characterized by FE-SEM. Additionally, the cross-linking degree of the PA membrane increased from 50.8 to 83.2%, as detected by XPS, with the detailed data presented in Figures 4b and S8−S11. As shown in Figure S5, at low TBDA concentrations of 0.5 mg·mL^{-1}, a defective PA selective layer is formed. As the TBDA concentration increases, more monomers participate in the reaction, promoting the formation of a defect-free membrane. As the TBDA concentration was further increased from 2.0 to 4.0 mg·mL^{-1}, the H_2/CO_2 selectivity of the membrane decreased from 23.5 to 15.3. Additionally, the gas permeance dropped from 160 to 25.4 GPU as the membrane thickness increased from 95 to 140 nm, as characterized by FE-SEM, as shown in Figure S6. When the TBDA concentration was fixed at 2.0 mg·mL^{-1}, increasing the TMC concentration from 1.0 to 8.0 mg·mL^{-1} resulted in a gradual increase in membrane thickness from 95 to 110, 125, and 145 nm, as shown in Figures 5 and S7. As summarized in Figure 4c, the H_2/CO_2 selectivity of the membrane decreased from 23.5 to 18.7, and the permeance of the membranes dropped from 160 to 62 GPU. The cross-linking degree of the PA membranes varied between 83.2 and 76.1%, with minimal change detected by

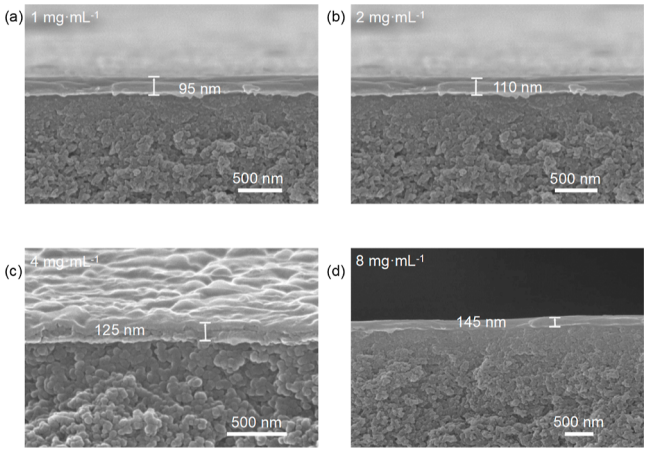

Figure 5. Cross-sectional FE-SEM images of PA-TBDA membranes with varying TMC concentrations. Images show PA-TBDA membranes with TMC concentrations of (a) 1.0, (b) 2.0, (c) 4.0, and (d) 8.0 mg·mL^{-1}, while the TBDA concentration was kept constant at 2.0 mg·mL^{-1}.

XPS, as shown in Figure 4d and Figure S12−S14. Based on the experimental results, the optimal monomer concentrations are determined to be 2.0 mg·mL^{-1} for TBDA and 1.0 mg·mL^{-1} for TMC. The corresponding H_2 permeance and mixed-gas H_2/CO_2 selectivity of the membranes are 160 GPU and 23.5, respectively. Additional data on gas permeance and H_2/CO_2 selectivity for the membrane are summarized in Table S3. Figure S15 shows how the membrane thickness affects the gas separation properties of PA-TBDA membranes. The gas permeance decreases sharply from 160 to 37 GPU with

https://doi.org/10.1021/acs.macromol.4c00967
Macromolecules 2024, 57, 9419−9428

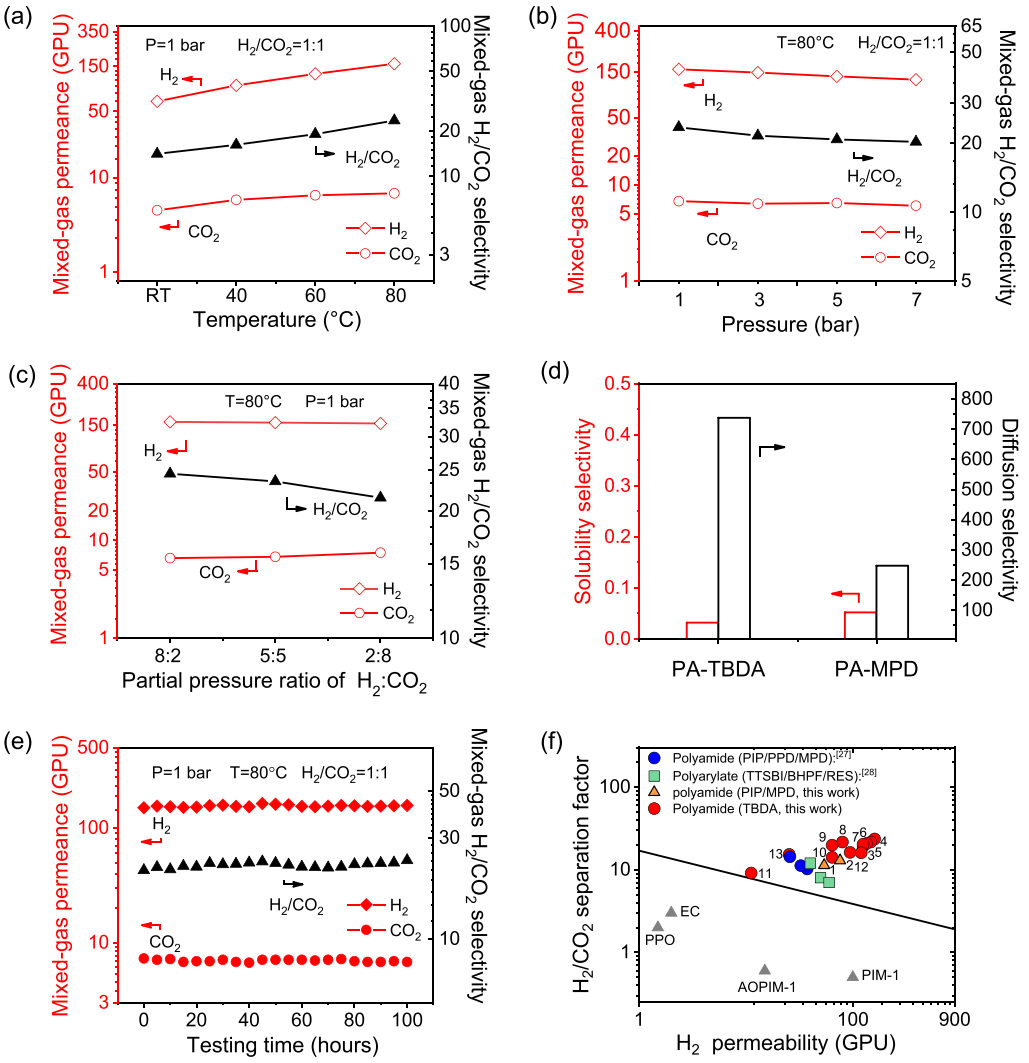

Figure 6. Performance and stability of PA-TBDA membranes for H_2/CO_2 separation. Impact of (a) feed temperature, (b) feed pressure, and (c) volume ratio of mixed H_2 and CO_2 feed gas on the separation efficiency of PA-TBDA membranes. (d) Solubility selectivity and diffusion selectivity of the PA-TBDA and PA-MPD membranes. (e) Long-term separation performance of PA-TBDA membranes for H_2/CO_2. (f) Comprehensive summary of H_2/CO_2 mixed gas separation performances of PA-TBDA membranes (TMC = 1 mg·mL^{-1}, TBDA = 2 mg·mL^{-1}, test pressure = 1 bar, 1-RT, 2–40, 3–60, 4–80 °C; TMC = 1 mg·mL^{-1}, TBDA = 2 mg·mL^{-1}, test temperature = 80 °C, 5–3, 6–5, 7–7 bar; TBDA = 2 mg·mL^{-1}, test pressure = 1 bar, test temperature = 80 °C, 8-TMC-2 mg·mL^{-1}, 9-TMC-4 mg·mL^{-1}, 10-TMC-8 mg·mL^{-1}; TMC = 1 mg·mL^{-1}, test pressure = 1 bar, test temperature = 80 °C, 11-TBDA-0.5 mg·mL^{-1}, 12-TBDA-1 mg·mL^{-1}, 13-TBDA-4 mg·mL^{-1}). The results are compared with the most commonly used commercial membranes and state-of-the-art polymer membranes prepared via spin coating, with reference to the Robeson upper bound in 2008: PA (PIP/PPD/MPD),[27] polyacrylate (TTSBI/BHPF/RES).[28]

increasing membrane thickness, as characterized by FE-SEM, as shown in Figures S16 and S17.

The H_2/CO_2 separation performance of the membrane, with the optimal physicochemical structure (2.0 mg·mL^{-1} for TBDA and 1.0 mg·mL^{-1} for TMC), was further assessed under various testing conditions. These details are summarized in Table S4. Figure 6a illustrates the effect of the feed temperature on the H_2/CO_2 separation performance of the membranes. As the temperature rises from room temperature to 80 °C, the gas permeance increases significantly from 64 to 160 GPU, and the H_2/CO_2 selectivity rises from 14 to 23. Figure 6b shows the effect of the feed pressure on the H_2/CO_2 separation performance of the membranes. As the feed pressure increases from 1 to 7 bar at 80 °C, the gas permeances decrease from 160 to 125 GPU, while the H_2/CO_2 selectivity of the PA-TBDA membranes slightly decreases from 23.5 to 20.3. To further investigate the antiplasticization performance of the PA-TBDA membranes, the CO_2 pressure was gradually increased from 3 to 33 bar to assess the gas permeability of the membranes, as shown in Figure S18. When the pressure is increased to 33 bar, there is still no evidence of plasticization, demonstrating that PA-TBDA membranes exhibit excellent plasticization resistance. Figure 6c illustrates the effect of the volume ratio on the H_2/CO_2 separation performance of the membranes. As the volume ratio of H_2:CO_2 decreases, the CO_2 permeance increases, while the H_2/CO_2 selectivity decreases. This is likely due to the increased competitive adsorption capacity of CO_2 molecules as the proportion of CO_2 in the feed gas. To gain a deeper understanding of the gas transport mechanism in PA-TBDA membranes, the solubility coefficient (S) and diffusion coefficient (D) were calculated and are listed in Table S5. For comparison, data for the PA-MPD membranes are also summarized. The solubility coefficient S_{H_2} of the PA-TBDA

https://doi.org/10.1021/acs.macromol.4c00967
Macromolecules 2024, 57, 9419−9428

membranes is 0.07 × 10^{-1} cm^3 (STP)/cm^3·cmHg, which is lower than 2.09 × 10^{-1} cm^3 (STP)/cm^3·cmHg for their S_{CO_2}. The S_{H_2} of PA-MPD membranes is 0.04 × 10^{-1} cm^3 (STP)/cm^3·cmHg, significantly lower than 0.84 × 10^{-1} cm^3 (STP)/cm^3·cmHg observed for their S_{CO_2}. In contrast, the diffusion coefficient D_{H_2} of PA-TBDA membranes is 14.39 × 10^{-9} cm^2/s, considerably higher than 0.02 × 10^{-9} cm^2/s measured for their D_{CO_2}. The D_{H_2} of PA-MPD membranes is 10.46 × 10^{-9} cm^2/s, which is significantly higher compared to 0.04 × 10^{-9} cm^2/s observed for their D_{CO_2}. This indicates that the solubility coefficient primarily influences the permeance of CO_2, whereas the permeance of H_2 is governed by the diffusion coefficient in both types of membranes. The H_2/CO_2 solubility selectivity (S_{H_2/CO_2}) and diffusion selectivity (D_{H_2/CO_2}) of the membranes are presented in Figure 6d. S_{H_2/CO_2} values for the PA-TBDA and PA-MPD membranes are 0.03 and 0.05, respectively. The D_{H_2/CO_2} selectivity values for the PA-TBDA and PA-MPD membranes are 737.35 and 247.44, respectively. This indicates that in both membranes, the selectivity is primarily governed by the diffusion selectivity. Additionally, the PA-TBDA membrane exhibits a more effective diffusion-controlled separation mechanism.

The long-term stability of the PA-TBDA membrane at 80 °C and 1 bar was evaluated using a 50:50 (vol/%) H_2 and CO_2 mixed gas feed. As illustrated in Figure 6e and detailed in Table S6, the PA-TBDA membrane was tested under these conditions for 100 h. During this period, the H_2 permeance and H_2/CO_2 selectivity remained approximately at 160 GPU and 21.5, respectively, demonstrating the membrane's stable and durable performance. The exceptional operational stability can be attributed to the hydrogen-bond-reinforced PA network structure. The separation performance of the PA-TBDA membranes is summarized and compared against the 2008 Robeson upper bound. As depicted in Figure 6f, the H_2/CO_2 selectivity of various PA-TBDA membranes significantly outperformed that of many commonly used commercial membranes, such as PBI (∼10) and polyether sulfone (PSF, ∼5). The comprehensive H_2/CO_2 separation performance of PA-TBDA membranes largely surpasses the 2008 Robeson upper bound. We also fabricated PA membranes containing PIP and MPD monomers using a fabrication method similar to that for PA-TBDA and measured their H_2/CO_2 separation performance. Their data points are displayed in the upper bound plot for comparison. The PA-TBDA membranes displayed much higher positions than them. Our PA-TBDA membranes also demonstrate superior H_2 permeance while getting a better H_2/CO_2 separation factor in comparison with those of other reported IP-based polymer membranes, including PA (PIP/PPD/MPD) and polyacrylate (TTSBI/BHPF/RES).

CONCLUSIONS

In summary, a series of hydrogen-bonded porous PA membranes were developed by incorporating TBDA through IP. The optimized separation performance was attained by fine-tuning the cross-linking degree and membrane thickness. FE-SEM, ^{13}C NMR, ATR-IR, XPS, TGA, physisorption, and WAXD techniques were employed to confirm the successful fabrication of the PA and characterize its pore structure. The unique contorted structure of TBDA enhances the micro-porosity of the resulting PA. Notably, strong hydrogen bonds form between the N atoms of TB and the H atoms of amide groups, which control the pore sizes of the created cavities. As a result, more H_2-selective channels are generated in the PA-TBDA membranes, enhancing gas selectivity while maintaining high H_2 permeance. The synergistic design of the micropore structure in the PA-TBDA membrane results in an outstanding H_2/CO_2 separation performance. The membrane demonstrates an exceptional H_2 permeance of 160 GPU and an impressive H_2/CO_2 selectivity of 23.5 at 353 K. It effectively overcomes the traditional trade-off between permeance and selectivity, achieving both high permeance and selectivity simultaneously. Additionally, the PA-TBDA membranes maintain stable separation performance for over 100 h. The hydrogen-bond-enhanced porous PA membranes demonstrate significant potential for H_2/CO_2 separation, substantially improving hydrogen purification efficiency. This breakthrough represents a major advancement in hydrogen purification technology, paving the way for more efficient and sustainable energy solutions.

ASSOCIATED CONTENT

Supporting Information

The Supporting Information is available free of charge at https://pubs.acs.org/doi/10.1021/acs.macromol.4c00967.

TGA curves; FE-SEM images; XPS and high-resolution spectra of C 1s, N 1s, and O 1s for the PA-TBDA membranes; diffusion coefficient data and solubility coefficient data of H_2 and CO_2 of PA-TBDA membranes; mixed-gas H_2 and CO_2 permeability; and H_2/CO_2 selectivity data tested at different test conditions (PDF)

AUTHOR INFORMATION

Corresponding Author

Zhenggong Wang − *College of Chemistry, Chemical Engineering and Materials Science & Collaborative Innovation Center of Suzhou Nano Science and Technology & Innovation Center for Chemical Science, Soochow University, Suzhou 215123, China; Jiangsu Key Laboratory of Advanced Negative Carbon Technologies and Jiangsu Key Laboratory of Advanced Functional Polymer Design and Application, Soochow University, Suzhou 215123, China;* orcid.org/0000-0003-1671-1803; Email: zgwang2017@suda.edu.cn

Authors

Yu Zhang − *College of Chemistry, Chemical Engineering and Materials Science & Collaborative Innovation Center of Suzhou Nano Science and Technology & Innovation Center for Chemical Science, Soochow University, Suzhou 215123, China*

Feng Zhang − *College of Chemistry, Chemical Engineering and Materials Science & Collaborative Innovation Center of Suzhou Nano Science and Technology & Innovation Center for Chemical Science, Soochow University, Suzhou 215123, China; Jiangsu Key Laboratory of Advanced Negative Carbon Technologies and Jiangsu Key Laboratory of Advanced Functional Polymer Design and Application, Soochow University, Suzhou 215123, China*

Shuqi Liu − *College of Chemistry, Chemical Engineering and Materials Science & Collaborative Innovation Center of*

Suzhou Nano Science and Technology & Innovation Center for Chemical Science, Soochow University, Suzhou 215123, China

Lele Guo − *College of Chemistry, Chemical Engineering and Materials Science & Collaborative Innovation Center of Suzhou Nano Science and Technology & Innovation Center for Chemical Science, Soochow University, Suzhou 215123, China*

Jian Jin − *College of Chemistry, Chemical Engineering and Materials Science & Collaborative Innovation Center of Suzhou Nano Science and Technology & Innovation Center for Chemical Science, Soochow University, Suzhou 215123, China; Jiangsu Key Laboratory of Advanced Negative Carbon Technologies and Jiangsu Key Laboratory of Advanced Functional Polymer Design and Application, Soochow University, Suzhou 215123, China;* orcid.org/0000-0003-0429-300X

Complete contact information is available at: https://pubs.acs.org/10.1021/acs.macromol.4c00967

Author Contributions

Y.Z. and F.Z. contributed equally to this work. Z.W. conceived the original idea and supervised the project. Y.Z., F.Z., and S.L. performed the synthesis and characterization experiments. Y.Z., F.Z., S.L., L.G., J.J., and Z.W. wrote the manuscript. All authors discussed the results and commented on the manuscript.

Notes

The authors declare no competing financial interest.

■ ACKNOWLEDGMENTS

This work was supported by the National Natural Science Foundation of China (22378282 and 21988102), Gusu Innovation and Entrepreneurship Leading Talent Plan (ZXL2023189), the Natural Science Foundation of the Jiangsu Higher Education Institutions of China (23KJB150029), and the Key Development Project of Jiangsu Province (BE2022056).

■ REFERENCES

(1) Zhu, L. X.; Huang, L.; Venna, S. R.; Blevins, A. K.; Ding, Y. F.; Hopkinson, D. P.; Swihart, M. T.; Lin, H. Q. Scalable polymeric few-nanometer organosilica membranes with hydrothermal stability for selective hydrogen separation. *ACS Nano* **2021**, *15*, 12119−12128.

(2) Ali, Z.; Pacheco, F.; Litwiller, E.; Wang, Y.; Han, Y.; Pinnau, I. Ultra-selective defect-free interfacially polymerized molecular sieve thin-film composite membranes for H_2 purification. *J. Mater. Chem. A* **2018**, *6*, 30−35.

(3) Yang, T. X.; Xiao, Y. C.; Chung, T. S. Poly-/metal-benzimidazole nano-composite membranes for hydrogen purification. *Energy Environ. Sci.* **2011**, *4*, 4171−4180.

(4) Cong, S. Z.; Yuan, Y.; Wang, J. X.; Wang, Z.; Liu, X. L. Network polyimide membranes prepared by interfacial polymerization for hot H_2 purification. *AIChE J.* **2023**, *69*, No. e17983.

(5) Zhang, B.; Zhang, S. X.; Yao, R.; Wu, Y. H.; Qiu, J. S. Progress and prospects of hydrogen production: Opportunities and challenges. *J. Electron. Sci. Technol.* **2021**, *19*, 100080.

(6) Zhu, M. S.; Ai, X. M.; Fang, J. K.; Wu, K. J.; Zheng, L. F.; Wei, L. A.; Wen, J. Y. Optimal integration of electrolysis, gasification and reforming for stable hydrogen production. *Energy Convers. Manage.* **2023**, *292*, 117400.

(7) Chen, G. X.; Tu, X.; Homm, G.; Weidenkaff, A. Plasma pyrolysis for a sustainable hydrogen economy. *Nat. Rev. Mater.* **2022**, *7*, 333−334.

(8) Shabbani, H. J. K.; Othman, M. R.; Al-Janabi, S. K.; Barron, A. R.; Helwani, Z. H_2 purification employing pressure swing adsorption process: Parametric and bibliometric review. *Int. J. Hydrogen Energy* **2024**, *50*, 674−699.

(9) Bernardo, G.; Araújo, T.; da Silva Lopes, T.; Sousa, J.; Mendes, A. Recent advances in membrane technologies for hydrogen purification. *Int. J. Hydrogen Energy* **2020**, *45* (12), 7313−7338.

(10) Naquash, A.; Qyyum, M. A.; Chaniago, Y. D.; Riaz, A.; Yehia, F.; Lim, H.; Lee, M. Separation and purification of syngas-derived hydrogen: A comparative evaluation of membrane- and cryogenic-assisted approaches. *Chemosphere* **2023**, *313*, 137420.

(11) Chen, X. L.; Fan, Y. F.; Wu, L.; Zhang, L. Z.; Guan, D.; Ma, C. H.; Li, N. W. Ultra-selective molecular-sieving gas separation membranes enabled by multi-covalent-crosslinking of microporous polymer blends. *Nat. Commun.* **2021**, *12*, 6140.

(12) Sidhikku Kandath Valappil, R.; Ghasem, N.; Al-Marzouqi, M. Current and future trends in polymer membrane-based gas separation technology: A comprehensive review. *J. Ind. Eng. Chem.* **2021**, *98*, 103−129.

(13) Ding, L.; Wei, Y. W.; Li, L. B.; Zhang, T.; Wang, H. H.; Xue, J.; Ding, L. X.; Wang, S. Q.; Caro, J.; Gogotsi, Y. MXene molecular sieving membranes for highly efficient gas separation. *Nat. Commun.* **2018**, *9*, 155.

(14) Yong, W. F.; Zhang, H. Recent advances in polymer blend membranes for gas separation and pervaporation. *Prog. Mater. Sci.* **2021**, *116*, 100713.

(15) Lin, H. Q.; Ding, Y. F. Polymeric membranes: Chemistry, physics, and applications. *J. Polym. Sci.* **2020**, *58*, 2433−2434.

(16) Liu, W.; Jiang, S. D.; Yan, Y. G.; Wang, W. S.; Li, J.; Leng, K.; Japip, S.; Liu, J. T.; Xu, H.; Liu, Y. P.; Park, I. H.; Bao, Y.; Yu, W.; Guiver, M. D.; Zhang, S.; Loh, K. P. A solution-processable and ultra-permeable conjugated microporous thermoset for selective hydrogen separation. *Nat. Commun.* **2020**, *11*, 1633.

(17) Shan, M. X.; Liu, X. L.; Wang, X. R.; Liu, Z. L.; Iziyi, H.; Ganapathy, S.; Gascon, J.; Kapteijn, F. Novel high performance poly(p-phenylene benzobisimidazole) (PBDI) membranes fabricated by interfacial polymerization for H_2 separation. *J. Mater. Chem. A* **2019**, *7*, 8929−8937.

(18) Zhu, L. X.; Swihart, M. T.; Lin, H. Q. Tightening polybenzimidazole (PBI) nanostructure via chemical cross-linking for membrane H_2/CO_2 separation. *J. Mater. Chem. A* **2017**, *5*, 19914−19923.

(19) Cong, S. Z.; Wang, J. X.; Wang, Z.; Liu, X. L. Polybenzimidazole (PBI) and benzimidazole-linked polymer (BILP) membranes. *Green Chem. Eng.* **2021**, *2*, 44−56.

(20) Bitter, J. H.; Asadi Tashvigh, A. Recent advances in polybenzimidazole membranes for hydrogen purification. *Ind. Eng. Chem. Res.* **2022**, *61*, 6125−6134.

(21) Omidvar, M.; Nguyen, H.; Huang, L.; Doherty, C. M.; Hill, A. J.; Stafford, C. M.; Feng, X. S.; Swihart, M. T.; Lin, H. Q. Unexpectedly strong size-sieving ability in carbonized polybenzimidazole for membrane H_2/CO_2 separation. *ACS Appl. Mater. Interfaces* **2019**, *11*, 47365−47372.

(22) Naderi, A.; Asadi Tashvigh, A.; Chung, T. S.; Weber, M.; Maletzko, C. Molecular design of double crosslinked sulfonated polyphenylsulfone/polybenzimidazole blend membranes for an efficient hydrogen purification. *J. Membr. Sci.* **2018**, *563*, 726−733.

(23) Luan, L. P.; Shi, P. X.; Wang, Z.; Kapteijn, F.; Liu, X. L. Random organic framework membranes with hierarchical channels for H_2 separation. *J. Membr. Sci.* **2024**, *694*, 122420.

(24) Hu, L. Q.; Bui, V. T.; Fan, S. H.; Guo, W. J.; Pal, S.; Ding, Y. F.; Lin, H. Q. Supramolecular assemblies of polybenzimidazole and aromatic polycarboxylic acids with superior mechanical and H_2/CO_2 separation properties. *J. Mater. Chem. A* **2022**, *10*, 10872−10879.

(25) Omidvar, M.; Stafford, C. M.; Lin, H. Q. Thermally stable cross-linked P84 with superior membrane H_2/CO_2 separation properties at 100 °C. *J. Membr. Sci.* **2019**, *575*, 118−125.

(26) Ge, C. Q.; Sheng, M. L.; Yuan, Y.; Shi, F.; Yang, Y.; Zhao, S.; Wang, J. X.; Wang, Z. Recent advances of the interfacial polymer-

ization process in gas separation membranes fabrication. *J. Membr. Sci.* **2023**, *683*, 121854.
(27) Ali, Z.; Wang, Y. G.; Ogieglo, W.; Pacheco, F.; Vovusha, H.; Han, Y.; Pinnau, I. Gas separation and water desalination performance of defect-free interfacially polymerized para-linked polyamide thin-film composite membranes. *J. Membr. Sci.* **2021**, *618*, 118572.
(28) Jimenez-Solomon, M. F.; Song, Q. L.; Jelfs, K. E.; Munoz-Ibanez, M.; Livingston, A. G. Polymer nanofilms with enhanced microporosity by interfacial polymerization. *Nat. Mater.* **2016**, *15*, 760−767.
(29) Hu, L. Q.; Pal, S.; Nguyen, H.; Bui, V.; Lin, H. Q. Molecularly engineering polymeric membranes for H_2/CO_2 separation at 100−300 °C. *J. Polym. Sci.* **2020**, *58*, 2467−2481.
(30) Gao, A. T.; Yan, X. R.; Cong, S. Z.; Wang, X. Y.; Liu, H. F.; Wang, Z.; Liu, X. L. Designed channels in thin benzimidazole-linked polymer membranes for hot H_2 purification. *J. Membr. Sci.* **2023**, *668*, 121293.
(31) Guo, Z. C.; Cong, S. Z.; Luan, L. P.; Li, M.; Luo, C. L.; Wang, C. X.; Wang, Z.; Liu, X. L. Molecular-scale hybrid membranes: Metal-oxo cluster crosslinked benzimidazole-linked polymer membranes for superior H_2 purification. *AIChE J.* **2023**, *69*, No. e18226.
(32) Yan, X. R.; Song, T. Q.; Li, M.; Wang, Z.; Liu, X. L. Sub-micro porous thin polymer membranes for discriminating H_2 and CO_2. *Nat. Commun.* **2024**, *15*, 628.
(33) Tröger, J. Ueber Einige Mittelst Nascirenden Formaldehydes Entstehende Basen. *J. Prakt. Chem.* **1887**, *36*, 225−245.
(34) Rúnarsson, Ö. V.; Artacho, J.; Wärnmark, K. The 125th Anniversary of the Tröger's Base Molecule: Synthesis and Applications of Tröger's Base Analogues. *Eur. J. Org Chem.* **2012**, *2012*, 7015−7041.
(35) Carta, M.; Malpass-Evans, R.; Croad, M.; Rogan, Y.; Jansen, J. C.; Bernardo, P.; Bazzarelli, F.; McKeown, N. B. An efficient polymer molecular sieve for membrane gas separations. *Science* **2013**, *339*, 303−307.
(36) Zhuang, Y. B.; Seong, J. G.; Do, Y. S.; Jo, H. J.; Cui, Z. L.; Lee, J.; Lee, Y. M.; Guiver, M. D. Intrinsicallymicroporous soluble polyimides incorporating Tröger's base for membrane gas separation. *Macromolecules* **2014**, *47*, 3254−3262.
(37) Wang, Z. G.; Wang, D.; Zhang, F.; Jin, J. Tröger's base-based microporous polyimide membranes for high-performance gas separation. *ACS Macro Lett.* **2014**, *3*, 597−601.
(38) Wang, Z. G.; Isfahani, A. P.; Wakimoto, K.; Shrestha, B. B.; Yamaguchi, D.; Ghalei, B.; Sivaniah, E. Tuning the gas selectivity of tröger's base polyimide membranes by using carboxylic acid and tertiary base interactions. *ChemSusChem* **2018**, *11*, 2744−2751.
(39) Wang, Z. G.; Wang, D.; Jin, J. Microporous polyimides with rationally designed chain structure achieving high performance for gas separation. *Macromolecules* **2014**, *47*, 7477−7483.
(40) Qiao, X. Y.; Chung, T.-S. Diamine Modification of P84 Polyimide Membranes for Pervaporation Dehydration of Isopropanol. *AIChE J.* **2006**, *52*, 3462−3472.
(41) See Toh, Y. H.; Lim, F. W.; Livingston, A. G. Polymeric Membranes for Nanofiltration in Polar Aprotic Solvents. *J. Membr. Sci.* **2007**, *301*, 3−10.
(42) Ying, Y. P.; Yang, Z. Q.; Shi, D. C.; Peh, S. B.; Wang, Y. X.; Yu, X.; Yang, H.; Chai, K. G.; Zhao, D. Ultrathin covalent organic framework film as membrane gutter layer for high-permeance CO_2 capture. *J. Membr. Sci.* **2021**, *632*, 119384.
(43) Jiang, X.; Goh, K.; Wang, R. Air plasma assisted spray coating of Pebax-1657 thin-film composite membranes for post-combustion CO_2 capture. *J. Membr. Sci.* **2022**, *658*, 120741.
(44) Liang, J. C.; Wang, Z. G.; Huang, M. H.; Wu, S. S.; Shi, Y. S.; Zhang, Y. T.; Jin, J. Effects on carbon molecular sieve membrane properties for a precursor polyimide with simultaneous flatness and contortion in the repeat unit. *ChemSusChem* **2020**, *13*, 5531−5538.
(45) Wang, Z. G.; Ren, H. T.; Zhang, S. X.; Zhang, F.; Jin, J. Carbon molecular sieve membranes derived from tröger's base-based microporous polyimide for gas separation. *ChemSusChem* **2018**, *11*, 916−923.
(46) Wang, S. Y.; Wang, Z. G.; Zhu, S. W.; Liu, S. Q.; Zhang, F.; Jin, J. Highly porous ultrathin polyamide membranes for fast separation of small molecules from organic solvents. *J. Membr. Sci.* **2023**, *675*, 121540.
(47) Mao, G. Z.; Liu, T.; Chen, Y.; Gao, X.; Qin, J. C.; Zhou, H. L.; Jin, W. Q. Polyamide@GO microporous membrane with enhanced permeability for the molecular sieving of nitrogen over VOC. *J. Membr. Sci.* **2022**, *652*, 120443.
(48) Wu, S. S.; Liang, J. C.; Shi, Y. P.; Huang, M. H.; Bi, X. Y.; Wang, Z. G.; Jin, J. Design of interchain hydrogen bond in polyimide membrane for improved gas selectivity and membrane stability. *J. Membr. Sci.* **2021**, *618*, 118659.
(49) Guo, L. L.; Shi, Y. P.; Wu, S. S.; Jin, J.; Wang, Z. G. Poly(hydrazide-imide) membranes with enhanced interchain interaction for highly selective H_2/CO_2 separation. *Macromolecules* **2023**, *56*, 3430−3439.
(50) Wang, Z.; Ren, H.; Zhang, S.; Zhang, F.; Jin, J. Polymers of intrinsic microporosity/metal-organic framework hybrid membranes with improved interfacial interaction for high-performance CO_2 separation. *J. Mater. Chem. A* **2017**, *5* (22), 10968−10977.

https://doi.org/10.1021/acs.macromol.4c00967
Macromolecules 2024, 57, 9419−9428